Effect of pore architecture on magnetic-field-induced strain in polycrystalline Ni–Mn–Ga

X.X. Zhang [a,1], C. Witherspoon [b], P. Müllner [b], D.C. Dunand [a,*]

[a] *Department of Materials Science & Engineering, Northwestern University, Evanston, IL 60208, USA*
[b] *Department of Materials Science & Engineering, Boise State University, Boise, ID 83725, USA*

Abstract

Monocrystalline Ni–Mn–Ga alloys show magnetic-field-induced strains (MFIS) of up to 10% as a result of reversible twinning; by contrast, polycrystalline Ni–Mn–Ga shows near-zero MFIS due to strain incompatibilities at grain boundaries inhibiting twinning. Recently, we showed that porous polycrystalline Ni–Mn–Ga exhibits a small, but non-zero, MFIS value of 0.12% due to reduction of these incompatibilities by the porosity. Here, we study the effect of pore architecture on MFIS for polycrystalline Ni–Mn–Ga foams. Foams with a combination of large (~550 μm) and small (~80 μm) pores are fabricated by the replication method and exhibit thinner nodes and struts compared to foam containing only large (~430 μm) pores. When magnetically cycled, both types of foams exhibit repeatable MFIS of 0.24–0.28% without bias stress. As the cycle number increases from a few tens to a few thousands, the MFIS drops due to damage accumulation. The rate of MFIS decrease is lower in the dual-pore foam, as expected from reduced constraints on the twin boundary motion, since twins span the whole width of the thinner nodes and struts.
© 2010 Acta Materialia Inc. Published by Elsevier Ltd. All rights reserved.

Keywords: Magnetostriction; Porous material; Nickel alloys; Casting; Ni$_2$MnGa

1. Introduction

Shape memory alloys (SMA) are an important class of functional materials that can change their shapes and dimensions under the application of external fields [1–3]. The external fields used may be the thermal, electric or magnetic. Thermal activated SMA, such as Cu–Al–Ni, may exhibit plastic deformation of a few percent and thermally recoverable strains as large as 20% by heating the deformed martensite through the martensitic/austenitic transformation temperature [3]. However, the low thermal conductivity of bulk (>1 mm) and wire (0.1–1 mm diameter) SMA reduces their response frequency to the Hz range [4]. In contrast, piezoelectric materials, magnetostrictive materials and magnetic shape memory alloys (MSMA) may change their shapes in response to an electric and magnetic field at much higher frequency (kHz range). As compared to piezoelectric materials [5] and magnetostrictive materials such as Terfenol-D (Tb$_{0.27}$Dy$_{0.73}$Fe$_2$) [6], which generate strains in the range of 0.1%, MSMA can produce 10–100 times larger strains. MSMA include antiferromagnetic materials, such as Ni$_{45}$Co$_5$Mn$_{36.7}$In$_{13.3}$ [7], LaSrCuO [8] and Mn–Fe–Cu [9], and ferromagnetic materials, such as Fe–Pd, Fe–Pt [10] and Ni–Mn–Ga [11–13], among which the near-stoichiometric Ni$_2$MnGa alloy is the most promising and studied.

In 1996, Ullakko et al. [11] found a 0.2% magnetic-field-induced strain (MFIS) in a Ni–Mn–Ga single crystal and this alloy is a very promising material for use as an actuator, sensor [14–17] and voltage generator [18,19]. The MFIS of Ni–Mn–Ga single crystal increased from 1.3–4.3% in 1999 [20,21] to 2.3–6% in 2000 [22–24] and to 9.5% in 2002 [14,25]. The giant MFIS in a single crystal

* Corresponding author. Tel.: +1 847 491 5370.
E-mail address: dunand@northwestern.edu (D.C. Dunand).
[1] Present address: School of Materials Science & Engineering, Harbin Institute of Technology, West Dazhi Str. No. 92, Harbin 150001, China.

comes from twin boundary motion under the application of a magnetic field [13,15,22,26], which is driven by the magnetostress produced by the high magnetocrystalline anisotropy of the Ni–Mn–Ga alloy [11,13,22,27] and its low twinning stress [12,28–30]. The blocking stress required to suppress MFIS is 3–6 MPa [23,28], which is comparable to the maximum magnetostress available through a magnetic field. The factors affecting the mobility of twinning dislocations include the martensite crystal structure [27], internal and external constraints [31–35], and temperature [36,37]. External constraints result from mounting the sample in a holder and attaching strain gauges or other devices to the sample. Internal constraints include martensite variants, twin and grain boundaries, as well as point and line defects. The Ni–Mn–Ga alloy exhibits a cubic parent structure at elevated temperature, and transforms to pseudo-tetragonal five-layered (10 M), pseudo-orthorhombic seven-layered (14 M) or tetragonal non-modulated (NM) martensites when cooled through the martensite transformation temperature [27]. Unlike the cubic parent phase, which has a low magnetic anisotropy [38], 10 M, 14 M and NM martensites exhibit a high magnetic anisotropy, and 10 M and 14 M martensites have a low twinning stress (<0.1 MPa for 10 M [35] and ∼1 MPa for 14 M [39]), which leads to their high MFIS. In contrast, NM martensite has a higher twinning stress (6–18 MPa), which results in its low MFIS [39]. So the key strategies to enhance the MFIS of Ni–Mn–Ga alloy are to increase the magnetic anisotropy of the martensite, which is an inherent material property, and to decrease the constraints which prevent the twin boundary motion.

While for well-trained single crystals with one active twin system there are no internal constraints, one-dimensional internal constraints exist for fibers with a bamboo grain structure, two-dimensional internal constraints exist in ribbons with columnar grain structures [40] and three-dimensional internal constraints exist in bulk polycrystals. This is why high MFIS in Ni–Mn–Ga alloys has only been achieved in single crystals to date. However, fabrication of single crystal Ni–Mn–Ga alloy is slow (due to directional solidification) and unreliable (due to evaporation of Mn and chemical segregation). On the other hand, casting of polycrystalline Ni–Mn–Ga alloys is rapid and reliable, and thus much lower in cost.

Marioni et al. [41] theoretically show that 21% of the single-crystal MFIS can be reached in an assembly of randomly distributed Ni–Mn–Ga particles. In contrast to this promising theoretical prediction, the MFIS of Ni–Mn–Ga polycrystals without texture found in experiments is near-zero (i.e. 0.012% strain [32]) because of the strong constraints imposed by the grain boundaries. However, polycrystalline Ni–Mn–Ga with columnar grains created by solidification and annealing generated a 0.3% MFIS [42]. Later, unidirectional solidification was proved to be more efficient in producing textures in polycrystalline Ni–Mn–Ga and generating higher MFISs (i.e. 0.115% MFIS in polycrystalline Ni–Mn–Ga made by zone melting [43]

and 1% MFIS in textured Ni–Mn–Ga made by unidirectional solidification [44,45] followed by mechanical training [46]). In polycrystalline Ni–Mn–Ga wire [47] and thin film [48], where constraints are relaxed by surfaces, MFISs of 1.0% and 0.8% have been achieved.

Recently, we demonstrated that porosity increased the MFIS of polycrystalline Ni–Mn–Ga alloys whose austenite grains were grown into a bamboo structure spanning the width of the foam struts [31]. The MFIS was near-zero for a foam with 54% porosity but increased to 0.12% for a foam with 76% porosity; this latter strain, while small compared to that achieved in a single crystal, is similar to the strain of 0.2% exhibited by the best magnetostrictive materials, such as Terfenol-D [49]. Optical microscopy showed thinner nodes and struts in the high porosity foam, suggesting that reducing constraints and strain incompatibilities during magnetic-field-induced twinning is key to increasing the MFIS in porous polycrystalline Ni–Mn–Ga. Here, we further investigate this concept by creating foams with two populations of pores: (i) large pores (as in our previous work [31]), with a corresponding population of large Ni–Mn–Ga nodes and struts; and (ii) smaller pores, located within each larger node, which then shows a finer porous structure. In a previous publication [50], one such dual-porosity Ni–Mn–Ga foam with 62% porosity (and with a polycrystalline structure [51]) showed remarkably high MFIS values of 2.0–3.6% at ambient temperature, and an even higher value of 8.7% after multiple thermal cycles. Here, the processing, microstructure and MFIS properties are systematically investigated for polycrystalline dual-porosity Ni–Mn–Ga foams and compared to those of the previous foams with a single population of pores.

2. Experimental procedures

2.1. Foam fabrication

The Ni–Mn–Ga foams were created via the casting replication method [52] using sodium aluminate (NaAlO$_2$) as the space holder (chosen because of its high melting temperature of 1650 °C, excellent chemical stability with molten metals and good solubility in acid [53]), in a method similar to that previously used for foams with monosized pores [31]. First, relatively coarse NaAlO$_2$ powders were prepared, as described previously [53], by cold pressing NaAlO$_2$ powders (technical grade, purchased from Alfa Aesar, Ward Hill, MA) at 125 MPa and sintering at 1500 °C for 3 h in air, then breaking up the sintered body with a mortar and pestle. The resulting powder was sieved into three different size ranges, as shown in Fig. 1: 355–500 μm, used for foams with single pore size; and 75–90 and 500–600 μm, used, with a 27:73 mass ratio, for foams with two pore sizes. For the former specimen, the 355–500 μm powder was directly poured into a 9.7 mm diameter alumina crucible and slightly tapped to a height of 22.1 mm. For the latter specimens, the coarse and fine powders were poured alternately in small batches into a 9.7 mm
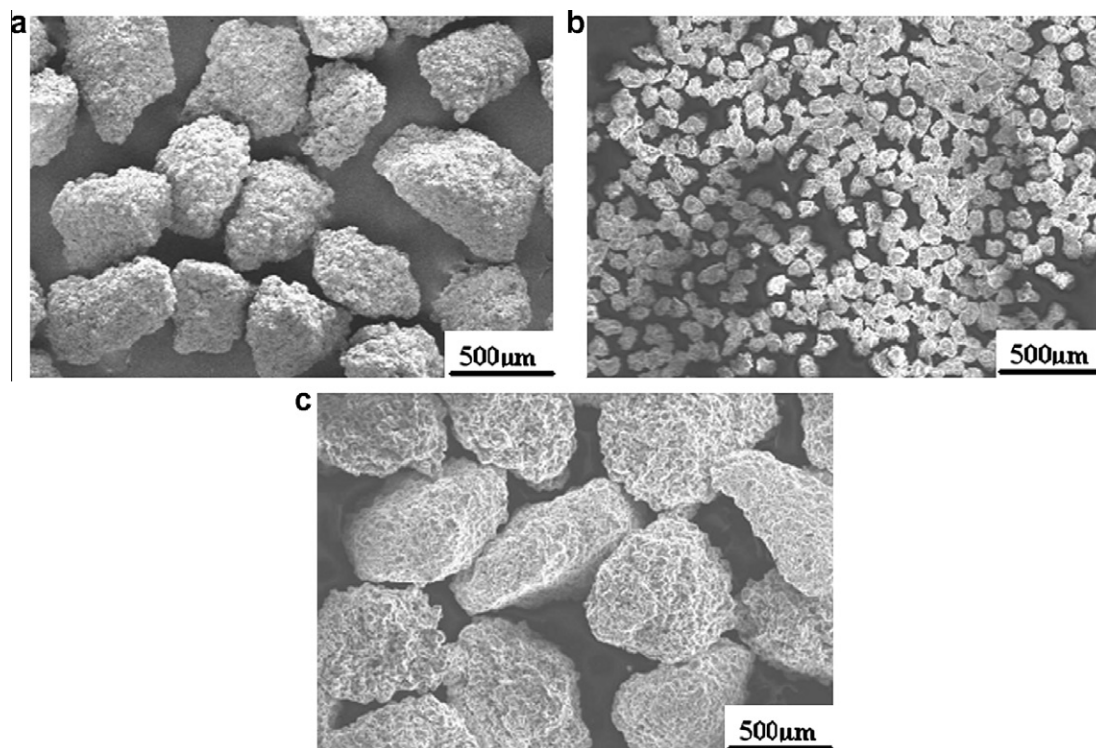
Fig. 1. SEM micrographs of NaAlO$_2$ powders with different sizes used as a space holder to prepare the Ni–Mn–Ga foams: (a) 355–500 μm powders, (b) 75–90 μm powders, (c) 500–600 μm powders.

diameter alumina crucible filled with acetone (which has no solubility for NaAlO$_2$): the 500–600 μm powder is first poured in a small 45.0 mg batch, followed by a 16.6 mg batch of 75–90 μm powder, which is allowed to settle in the space between the 500–600 μm powders from the previous batch. In this manner, the two batches of powders were well mixed, unlike dry mixing, which invariably led to powder size segregation. This process was repeated until the NaAlO$_2$ powder reached a height of 22 mm in the crucible. This latter crucible was heated at 70 °C overnight so that the acetone evaporated, then both crucibles were heated at 1500 °C for 3 h in air to partially sinter the NaAlO$_2$ powders into a percolating NaAlO$_2$ powder preform, which prevented powder pushing during infiltration and was subsequently removed by acid dissolution. The volume fractions of NaAlO$_2$ powders in the preforms containing single and bimodal powder sizes were 43% and 45%, respectively, as calculated from the volume and mass of the preforms.

Ni$_{52}$Mn$_{24.4}$Ga$_{23.6}$ (atomic percent) and Ni$_{51.3}$Mn$_{25.2}$Ga$_{23.5}$ billets, inductively melted from elements with purities of 99.9% for Ni, 99.95% for Mn and 99.999% for Ga (all metal basis, non-metal impurities were not specified), were cast into a copper mold and used respectively for infiltration of preforms with single and bimodal powder sizes. The billet was placed on top of the preform within the alumina crucible, which was then heated to 1200 °C (above the alloy melting temperature of 1125–1130 °C) at a rate of 7 °C min^{-1} under a vacuum of 3.5×10^{-6} Torr and maintained for 24 min at 1200 °C to ensure melting of the alloy. Then high-purity argon gas was introduced into the furnace to force the molten alloy into the porous preform at a 1.34 atm pressure, and the temperature was reduced from 1200 to 24 °C at 7 °C min^{-1}. The infiltrated Ni–Mn–Ga/NaAlO$_2$ composite was cut with a diamond saw into parallelepiped samples with dimensions of $x = 1.96$, $y = 3.13$ and $z = 6.08$ mm for the single powder specimen and $x = 2.06$, $y = 2.94$ and $z = 6.43$ mm for the dual powder specimen. These composite samples were homogenized at 1000 °C for 1 h in high vacuum and then subjected to a stepwise heat treatment to allow for chemical ordering establishing the L2$_1$ structure [31]: 2 h at 725 °C, 10 h at 700 °C and 20 h at 500 °C. The annealed composite samples with monosize NaAlO$_2$ powders were then immersed in a 10% HCl aqueous solution to dissolve, under sonication, the NaAlO$_2$ space holders. After 53.3 h of dissolution, a Ni–Mn–Ga foam with 56.6% porosity was achieved. The annealed composite with bimodal NaAlO$_2$ powders was first immersed for 14.5 h in a 34% H$_2$SO$_4$ aqueous solution in a sonication bath to remove the coarse NaAlO$_2$ powders in the foam and then immersed for 90.3 h in a 10% HCl aqueous solution to remove the fine NaAlO$_2$ powders and to further thin the struts. This foam achieved a porosity of 66.8%, ~10% higher than the foam with monosize NaAlO$_2$ powders (i.e. with a relative density decreased by one-quarter). The water in the sonicator bath was maintained at 24 °C and the acids were replaced every 2 h during sonication.

2.2. Microstructure and property characterization

Metallographic specimens were cut and prepared by vacuum infiltration of epoxy into the foam pores, which was hardened at 70 °C for 2 h. The specimens were then cold-mounted, mechanically ground with SiC paper and polished with 9, 3 and 0.5 μm alumina suspension. The polished surface before and after etching with Kalling Nr. 2 etchant was imaged with an Olympus optical microscope. The twins were made visible using polarizer and a Normarsky objective lens, with a quarter-wavelength plate. A Hitachi S3400N-II scanning electron microscope equipped with an integrated Oxford Electron Dispersive Spectrum system was used to characterize the $NaAlO_2$ powder and the foams. Compositions of the specimens were measured by scanning electron microscopy (SEM)–electron dispersive spectroscopy (EDS) using the same standard conditions (20 kV voltage, 97 μA emission current, 10 mm work distance and 50 μA probe current and data acquisition time >60 s). Precision of the composition measurement by EDS was calibrated with chemical analysis results of the same alloy and the measured errors were <±0.5%. The transformation temperature and Curie point were measured with a vibrating sample magnetometer (VSM; ADE Technologies Model 10) with a detection limit of $<1 \times 10^{-6}$ emu (corresponding to a resolution of 2×10^{-6} A m^2 kg^{-1}) under a magnetic field of 0.028 or 0.032 T, by heating the sample from 25 to 150 °C at 8.5 °C min^{-1}, maintaining this temperature for 5 min and cooling to 25 °C at 8.5 °C min^{-1}.

Thermo-magnetic training was carried out in the VSM under a magnetic field of 2 T: the sample was heated from 25 to 150 °C at 8.5 °C min^{-1} and kept at this temperature for 5 min, then cooled to 25 °C at 8.5 °C min^{-1} and kept at this temperature for 5 min. For the MFIS measurement, the foam was exposed to a rotating magnetic field $\mu_0 H = 0.97$ T while being glued at one end to a sample holder and at the other to a head capable of sliding in the direction of the foam z-axis only. The magnetic field rotational axis was parallel to the foam x-axis with the magnetic field vector rotating within the y–z plane [25]. The frequency of the rotating magnetic field – 4000 rpm during magneto-mechanical cycling – was reduced to 30 rpm during strain data acquisition to increase the accuracy. The foam minimum and maximum lengths along the z-axis were measured with an extensometer (Heidenhain, type MT1281) and transformed to MFIS values using the engineering definition of strain (i.e. the ratio of the elongation Δz to the original length z).

3. Results and discussion

3.1. $NaAlO_2$ removal and strut thinning

In our previous study of foams with monosize porosity [31], a 10% HCl solution was used, and was found to dissolve both the $NaAlO_2$ and, to a lesser extent, the alloy,

thus leading to strut thinning upon long exposure. For the present composites with dual $NaAlO_2$ space holder size, the thin struts separating the fine powders are dissolved by long exposure to the 10% HCl solution. Thus, in a first step, the coarse $NaAlO_2$ powders are removed without alloy dissolution, and in a second step, the remaining fine powders are removed with some thinning of the alloy. The acid for the first step should dissolve $NaAlO_2$ but not the Ni–Mn–Ga alloy, while the acid for the second step should dissolve $NaAlO_2$ rapidly and also Ni–Mn–Ga, albeit slowly, with the advantage of opening small fenestrations between the fine $NaAlO_2$ particles. Systematic experiments led to the selection of aqueous solutions with 34% sulfuric acid and 10% hydrochloride for these two steps. As shown in Fig. 2a, plots of mass loss vs. time for bulk, non-porous Ni–Mn–Ga are linear for these acids, with slopes corresponding to dissolution rates of 16 and 5 mg m^{-2} min^{-1} in 10% HCl and 34% H_2SO_4, respectively. Doubling the concentration to 20% HCl leads to a quadrupling of the dissolution rate to 62 mg m^{-2} min^{-1}, which was not used here as it may have dissolved the thin struts fully before completing the $NaAlO_2$ removal.

Fig. 2b shows a plot of mass loss vs. time for a foam sample with dual-size $NaAlO_2$ powder immersed in 34% H_2SO_4. For the first 650 min, the mass loss rate is high, corresponding to the dissolution of the coarse $NaAlO_2$ powders. The mass loss at the end of this first stage is 14% of the foam mass, corresponding to 71% of the $NaAlO_2$ mass present in the composite, which is in good agreement with the nominal 73% fraction of coarse $NaAlO_2$ particles. Considering the size of the sample with dual pores ($x = 1.96$, $y = 3.13$ and $z = 6.08$ mm) and the 500–600 μm size of the coarse powders, there are about four coarse powder particles along the smallest sample dimension of 1.96 mm, so that removal of the coarse powders is expected to be fairly rapid. Beyond this first stage, Fig. 2b shows that the mass loss rate is much reduced, as expected if the water and acid cannot easily reach (and the reaction products escape from) the fine $NaAlO_2$ powders connected with each other at small contact areas. As shown in Fig. 2b, tripling the immersion time to 2000 min increased the mass loss from 14% to 17%, which corresponds to an 87% removal of the $NaAlO_2$ from the composite (assuming no dissolution of the alloy).

A foam sample of similar dimensions ($x \approx 2$, $y \approx 3$ and $z \approx 6$ mm) and with the same $NaAlO_2$ double size distribution was first immersed in a 34% H_2SO_4 solution for 645 min (corresponding to the end of the rapid dissolution stage in Fig. 2b) and then transferred to a 10% HCl solution for further removal of the remaining fine $NaAlO_2$ particles and thinning of the struts. As shown in Fig. 2c, the foam porosity increases rapidly for the first 1140 min in the 10% HCl solution. The measured porosity of 55% at this point is higher than the original $NaAlO_2$ volume fraction of 45%, indicating that full removal of the fine $NaAlO_2$ particles and partial dissolution of the alloy took place. Further immersion to a total time of 4680 min increases
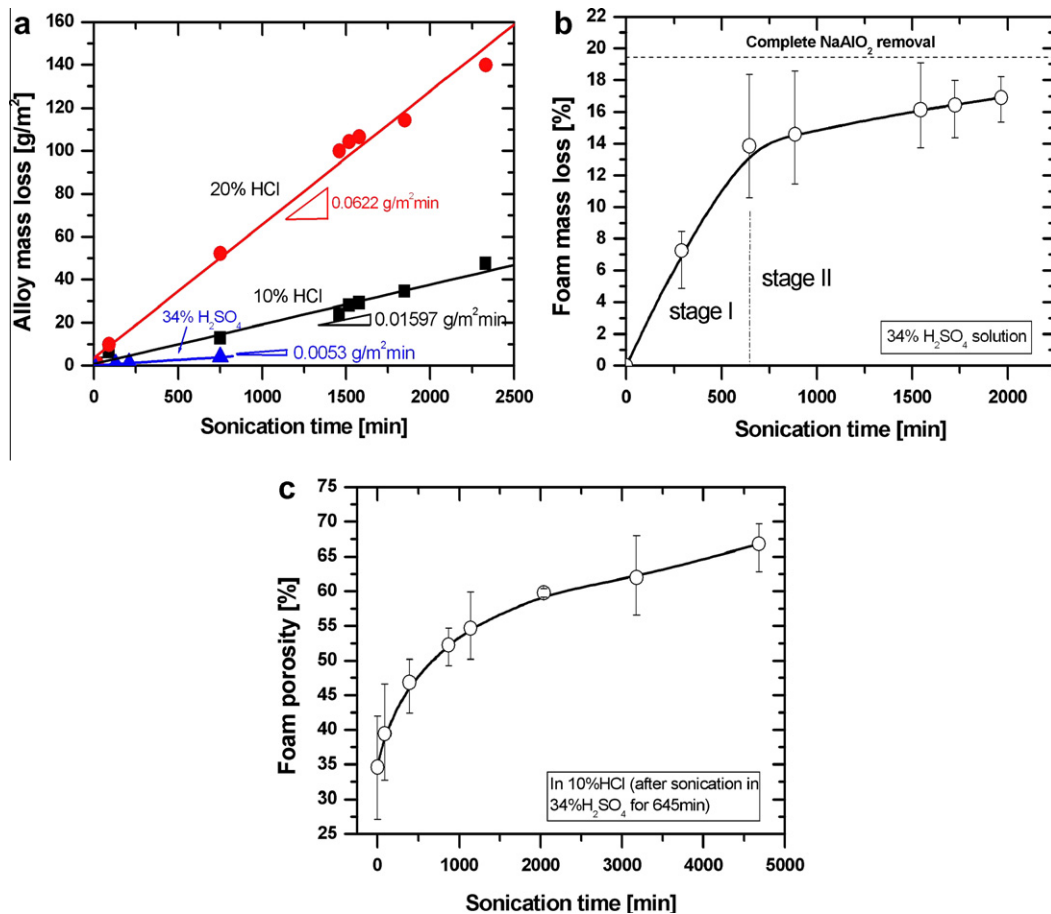
Fig. 2. (a) Plot of mass loss vs. time in bulk Ni–Mn–Ga alloy immersed in 10% and 20% HCl and 34% HNO_3 solutions under sonication; (b) plot of mass loss vs. time for foam with dual-size $NaAlO_2$ powders (1.96 × 3.13 × 6.08 mm) in 34% H_2SO_4 solution, showing two stages; (c) plot of foam porosity vs. time for foam with dual-size $NaAlO_2$ powders (2 × 3 × 6 mm) immersed in 10% HCl under sonication (following 645 min in 34% H_2SO_4).

the porosity to 67% at a much slower rate, indicating that the alloy alone is being dissolved, once the $NaAlO_2$ has been fully removed.

3.2. Pore architecture and twin morphology

The architecture of foam with open pores is described via struts which are connected through nodes. Struts with a non-equiaxed cross section can also be considered to be walls. Here, open pores are created after $NaAlO_2$ are removed, so the term "strut" is used. Polished cross-sections of the foams with single and dual pores are shown in Fig. 3. Foams with single pores exhibit nodes 100–200 μm in size and struts 40–100 μm in width and ~100 μm in length (Fig. 3a). In foams containing dual pores (Fig. 3b), the alloy between the large pores, which is solid in the previous foam (Fig. 3a), now contains small pores, thus producing a second population of smaller nodes and struts. It is apparent that the small pores are evenly distributed between the large pores, indicating that the blending of the fine and coarse powders was uniform. For both foams, very little casting porosity is visible within nodes or struts, implying that the infiltration process was complete.

SEM micrographs of cut and acid-etched surfaces further illustrate the open pore character of the foams, as shown in Fig. 4a–c. Fig. 4a shows the three-dimensional (3-D) structure of the single-pore foam with 56.6% porosity, illustrating the large nodes and struts. Fig. 4b shows the 3-D structure of the dual-pore foam, with a porosity of 66.8%. No remaining $NaAlO_2$ powders can be detected, and the small nodes and struts are undamaged by the acid treatment. Fig. 4c is an enlarged picture of Fig. 4b, showing fine parallel ridges, with a thickness of about 1 μm, on the nodes and struts. These ridges in Fig. 4c are probably the etched martensite twins intersecting the surface of the struts, as can be deduced by comparing with the twins in Fig. 5. Twin domains are clearly visible in Fig. 4c as well.

Polished cross-sections of the foam with dual pores are shown in Fig. 5, with polarized light making the twins visible. For the as-cast foam, ~1–5 μm wide twins cover the whole width of the small struts but not of the large struts (Fig. 5a). For the annealed foam (Fig. 5b), the twins are thicker (~5–10 μm in width) and have coarsened, thus increasing locally the magnetic anisotropy of the alloy. Surfaces act as sinks and sources of twinning dislocations and promote the mobility of twin boundaries. Generally, wider
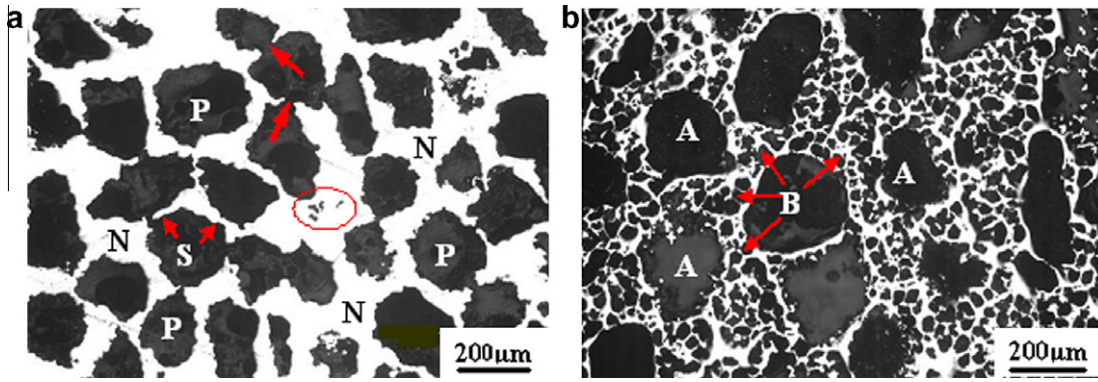
Fig. 3. Optical micrographs of polished cross-sections of Ni–Mn–Ga foams. Metal struts (S) and nodes (N) appear bright and the pores appear dark. (a) Foam with single pore size distribution, made with 355–500 μm $NaAlO_2$ powders. Contrast within the large (∼550 μm) pores (P) is due to their partial filling with epoxy used to achieve better edge retention during polishing. A few small pores due to solidification shrinkage are marked with a circle. Some of the struts are discontinuous (arrows). (b) Foam with dual pore size distribution, made with a blend of coarse (500–600 μm) and fine (75–90 μm) $NaAlO_2$ powders. Large (∼430 μm) and small (∼80 μm) pores are marked with A and B.
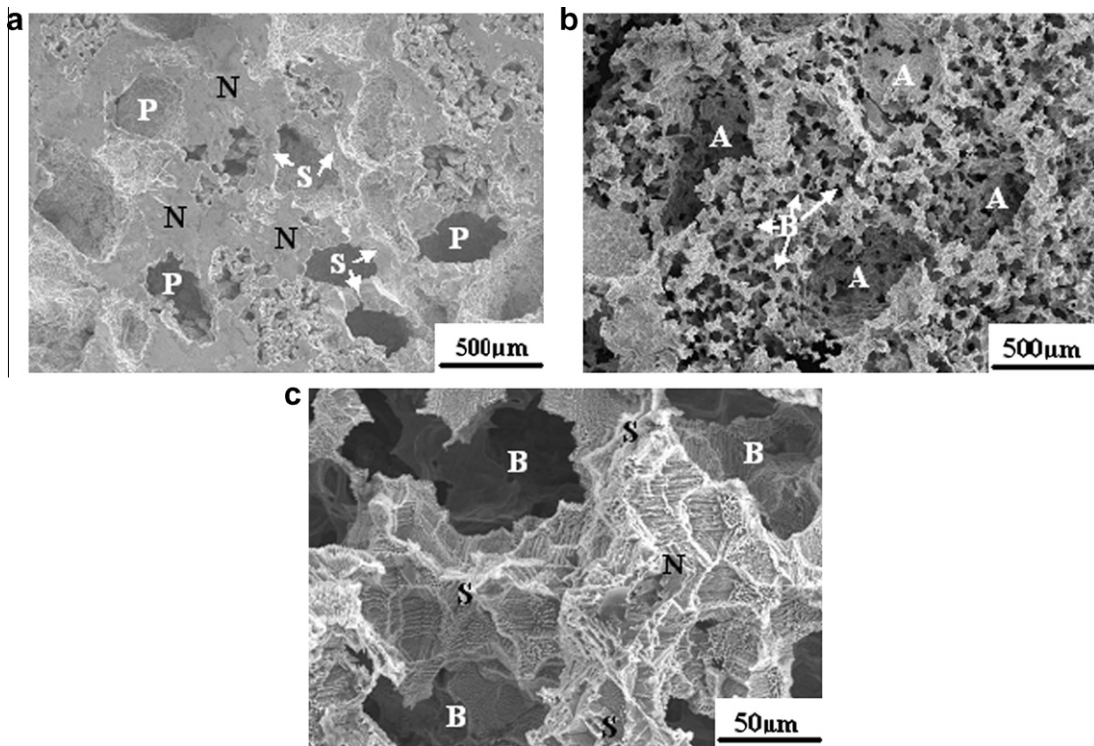

Fig. 4. SEM micrographs of cut and etched surface of Ni–Mn–Ga foams showing the three-dimensional structure and connectivity of pores. (a) Single-pore foam with pores (P), nodes (N) and struts (S) marked. (b) Dual-pore foam showing both types of large (A) and small (B) pores, which give rise to a dark contrast; the small pores (B) are within the large struts and nodes surrounding the large pores; (c) enlarged view of (b), showing etched ridges corresponding to twin variants with various orientations at nodes (N) and struts (S) surrounding small pores (B).

and longer twins spanning whole nodes and struts (such as in the annealed foam, Fig. 5b) are more mobile than thinner, shorter twins (such as in the as-cast foam, Fig. 5a), the mobility of which is inhibited by twin–twin interaction [54]. Thus, the MFIS is improved in the annealed foams.

3.3. Composition evolution

The transformation temperature and crystal structure of the Ni–Mn–Ga martensite phase affect the degree of MFIS.

Transformation temperature and martensite structure depend on the chemical composition [1], which must remain as constant as possible during processing. The compositional evolution during the fabrication of a foam with dual pores is shown in Fig. 6. The induction-melted billet has the composition $Ni_{51.3}Mn_{25.2}Ga_{23.5}$. After melting, infiltration and solidification, the excess alloy above the infiltrated composite has the composition $Ni_{50.8}Mn_{24.3}Ga_{24.9}$, with a slight Ni and Mn depletion and a concomitant slight Ga enrichment, compared to the original billet. In the foam
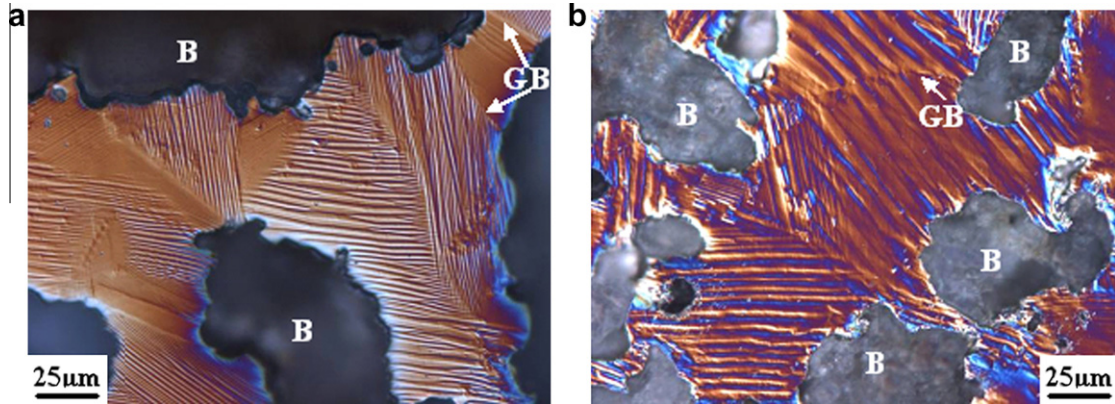
Fig. 5. Optical micrographs of polished cross-sections of dual-pore foam in area with small pores (B) imaged with polarized light. (a) As-cast state, with fine twins, many of which do not span the width of the struts. Bamboo grain exists on slender struts; (b) annealed state, with coarser twins spanning the whole width of the nodes and struts. A grain boundary (GB) at a node is also visible.
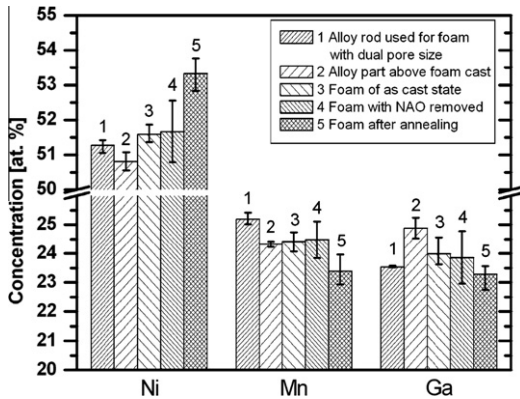

Fig. 6. Compositional evolution of dual-pore foam during processing.

area, the composition is $Ni_{51.6}Mn_{24.5}Ga_{23.9}$, which is closer to that of the billet, indicating a slight tendency for segregation along the foam billet axis during solidification. In the foam after $NaAlO_2$ removal by sulfuric and hydrochloride acids, the composition is unchanged within experimental error: $Ni_{51.7}Mn_{24.5}Ga_{23.8}$. However, after heat treating to achieve chemical ordering, the composition changed to $Ni_{53.3}Mn_{23.4}Ga_{23.3}$, showing an increase in Ni and a

decrease in Mn and Ga, probably due to evaporation of the latter two elements. Comparing with the as-cast billet, there is a 0.7% Mn loss in the as-cast foam (almost within measurement error) and a 1.8% Mn loss in the annealed foam.

For achieving MFIS at room temperature, a necessary (though not sufficient) condition is for the alloy to display the martensite-to-austenite transformation above room temperature. Furthermore, it was experimentally found that for MSMAs with large MFIS the martensitic transformation occurs below the Curie point. These conditions are fulfilled for both foams in the present study, as found from temperature-dependent magnetization measurements (Fig. 7). For the single-pore foam (Fig. 7a), the martensite-to-austenite transformation starts at 31 °C and finishes at 39.5 °C on heating, while the austenite-to-martensite transformation starts at 35 °C and finishes at 25 °C on cooling; its Curie point is 81 °C. For the dual-pore foam (Fig. 7b), the martensite transforms to austenite starting at 30 °C and finishing at 54 °C on heating and the austenite transforms to martensite starting at 52 °C and finishing at 27 °C on cooling. The Curie point of this foam is 82 °C. Thus, both foams show a martensitic–austenitic transformation temperature higher than room temperature,
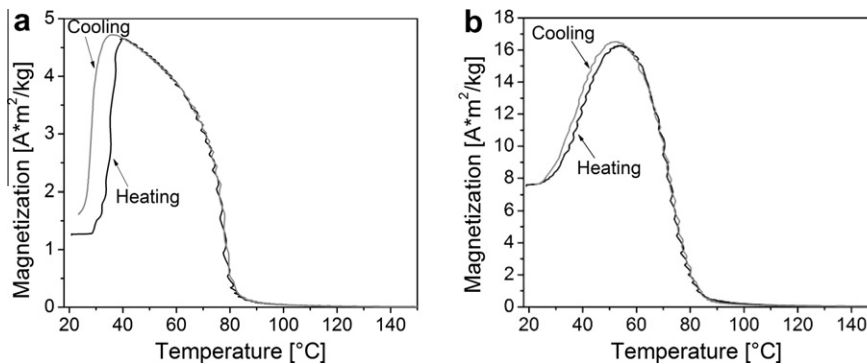

Fig. 7. Magnetization–temperature curve of Ni–Mn–Ga foam measured with a VSM. (a) Foam of the annealed state with single pores in a 0.0326 T magnetic field; (b) foam of the annealed state with dual pores in a 0.028 T magnetic field.

ensuring that the sample is martensitic at room temperature, permitting room-temperature MFIS. The transformation range of the dual-pore foam is much larger than the thermal hysteresis.

The temperature hysteresis of the austenitic and martensitic transformations is 4.5–6 °C for the single-pore foam, and only 2–3 °C for the dual-pore foam. This indicates spatial variations of stress and/or composition. This also reveals that the austenitic–martensitic transformation is more reversible in the latter foam, as expected if the finer and higher porosity reduce constraints for the nucleation of martensite/austenite during the phase transformation and for the motion of twin boundaries. The martensite transformation temperatures of both foams are quite close to the MFIS measurement temperature, which means that the martensite phase is compliant [55] and the twinning stress is low [39,56–58]. The transformation temperature ranges are also narrow, confirming that chemical composition is homogeneous.

3.4. Magnetic-field-induced strain

3.4.1. Single-pore foam

Fig. 8a and b shows plots of MFIS of the single-pore foam after annealing. Fig. 8a is a plot of MFIS vs. magneto-mechanical cycles (MMC), starting at cycle 78 (earlier MMC data were not acquired). The MFIS decreases from

Fig. 8. MFIS of single-pore foam with 56.6% porosity. (a) MFIS vs. MMC; (b) MFIS vs. magnetic field orientation for 68 and 20,378 MMC.

0.24% at cycle 78 to 0.18% at cycle 506, then remained stable at 0.18–0.19% until cycle 20,378. The MFIS decrease during the first thousand cycles is likely due to damage accumulation in the form of microcrack initiation and propagation by fatigue reducing the connectivity of the foam and thus the macroscopic strain. Pinning of twinning dislocations by elemental segregation or by the accumulation of twinning dislocations at twin boundaries may also occur during plastic deformation. Pinning lowers the mobility of twin boundaries and thus the MFIS. Finally, magneto-mechanical training in a rotating magnetic field may also be taking place but, if this is the case, the expected increase in MFIS was canceled by the damage mechanisms. Further systematic investigations are needed to isolate and quantify each of these factors.

Fig. 8b shows plots of MFIS vs. magnetic field orientation for cycles 68 and 20,378 for the same single-pore foam shown in Fig. 8a. The foam elongates and contracts four times during one 360° revolution of the magnetic field (which is 2 MMC): in the first MMC (0–180°), two strain peaks appear at ~60 and ~115°, with respective MFIS of 0.20% and 0.24% for 68 MMC. In the second MMC (181–360°), the same peaks occur at ~240 and ~300°, as expected. The occurrence of two strain peaks at ~60/240 and ~115/300° (rather than a single peak expected from a single crystal) reflects the polycrystalline nature of the foam, in which grains of different orientations in the foam nodes and struts elongate and contract in different directions, thus contributing differently to the average foam strain measured only in the z direction. The two strain peaks probably correspond to two dominant twin variants expanding and contracting at their specific magnetic field angle, but blocked and prevented from further motion as the magnetic field angle changes. As shown in Fig. 8b, the heights of these peaks are reduced to 0.16% and 0.18% for cycle 20,378, as discussed earlier. The peak shapes after 20,378 MMC are unchanged, except for a small shoulder at ~105° within the second ~135/315° peak. This indicates the presence of another small peak, corresponding to the creation of a third dominant twin variant activated during training.

3.4.2. Dual-pore foam

Fig. 9a and b depicts the MFIS of the dual-pore foam and is equivalent to Fig. 8a and b for the single-pore foam. Direct comparison is however hampered by the different porosities (56.6% for Fig. 8a and b and 66.8% for Fig. 9a and b). Fig. 9a shows plots of MFIS vs. MMC number for various states of the dual-pore foam. When tested in the initial annealed state, the foam shows a strain of 0.10%, decaying to 0.014% after 60,000 MMC and remaining at this value for up to ~300,000 MMC. After subsequent thermo-magnetic training, the foam showed a notable increase in MFIS to 0.28% for MMC 4, again decaying to 0.17% after 6000 MMC. The MFIS of 0.28% is over twice as large as the values reported in our previous study of single-pore foams [31], in which the MFIS
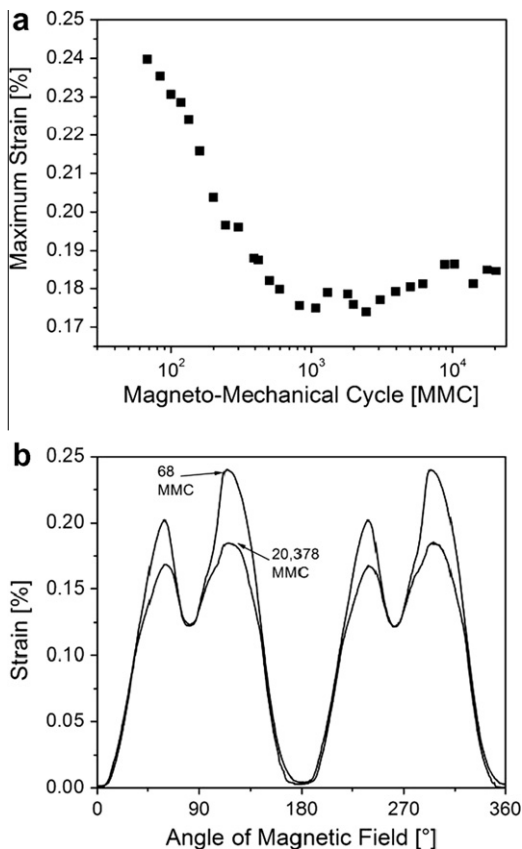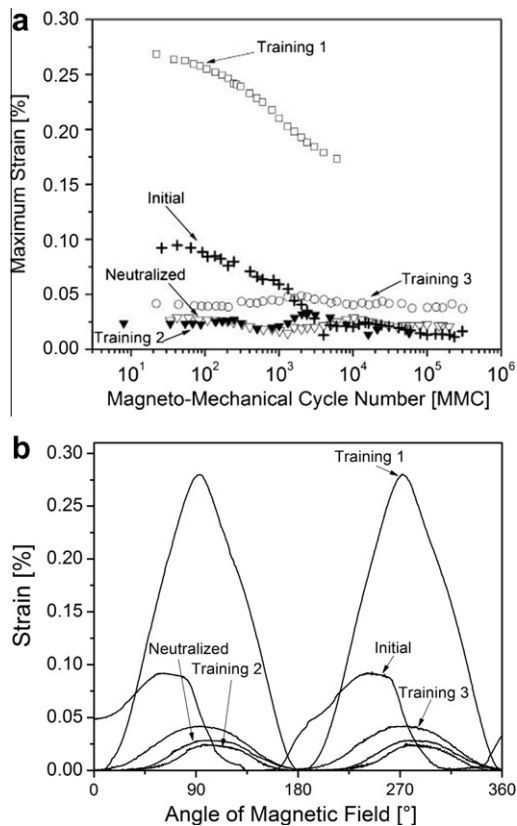
Fig. 9. MFIS of dual-pore foam with 66.8% porosity. (a) MFIS vs. MMC for five different states: as-annealed, first training, neutralized, second training and third training; (b) MFIS vs. magnetic field orientation for the same five states.

amounted to 0.01% for a foam with 54% porosity and to 0.12% for a foam with 76% porosity. It is also slightly larger than the value of the present single-pore foam (Fig. 8a and b), which shows an MFIS of 0.24% after 100 cycles. However, it is much less than the previously reported values of 2.0–3.6% achieved for another dual-pore foam with 62% porosity created by the same process [50]. These variations between the various foams probably reflect the effects of various combinations of grain orientations and sizes and grain boundary location, as well as pore, strut and node architecture. Unlike bulk polycrystalline Ni–Mn–Ga alloys [43–45], for which a strong texture is necessary to achieve comparable MFIS values (1%), these polycrystalline Ni–Mn–Ga foams achieve significant MFIS values without the deliberate introduction of a texture by unidirectional solidification, since they were furnace-solidified without thermal gradients. The MFIS values are comparable to the 0.2% strain exhibited by the workhorse magnetostrictive alloy Terfenol-D [49].

The thermo-magnetically trained dual-pore foam was heated above its transformation temperature (150 °C) and cooled without magnetic field to neutralize the training effect. As expected, the MFIS decreased (open triangles Fig. 9a), to a value of ∼0.027%, which shows a slight decrease beginning at ∼1300 MMC to ∼0.014% followed by a stable level of MFIS from 0.027 to 0.020% up to

∼200,000 MMC (Fig. 9a). This demonstrates that thermo-magnetic training can induce large MFIS in foams where the as-cast and annealed grain orientation does not initially allow for large MFIS values. The foam was then trained a second time, but the MFIS value did not increase significantly (Fig. 9a). Without another neutralization treatment, the sample was trained a third time, leading to a small strain increase to ∼0.04% (Fig. 9a), remaining near constant over ∼151,000 MMC. The increase in strain with additional training steps suggests that training may have an additive effect. The reason for the lack of response to the second and third training is not clear, but may result from damage (e.g. nodes and struts fracture) from the ∼805,000 magneto-mechanical cycles accumulated after the initial test, the first training test and the subsequent first neutralization test.

In the semi-logarithmic plots of Figs. 8a and 9a, the rate of MFIS decrease is roughly linear up to ∼500 and 6000 MMC in single- and dual-pore foams, respectively. The rate of strain decrease between 100 and 6000 MMC is ∼0.040 and 0.050% MMC^{-1} for the dual-pore foam in both annealed and trained states, respectively (Fig. 9a). This is lower than the value of ∼0.069% MMC^{-1} in the single-pore foam (Fig. 8a), indicating a higher resistance to damage in the dual-pore foam, which may be explained as follows. The dual-pore foam, with its smaller nodes and struts (Figs. 3 and 4), shows twins spanning the whole width of the nodes and struts (Fig. 5). Twin boundary motion is then easier, reducing the number of twin–twin interactions and the creation of cracks to relieve mismatch stresses. Also, cracks originating in the small struts do not propagate as far as those originating in the larger nodes and struts of the single-pore foam (i.e. pores may act as crack arrester). This mechanism was recently substantiated with X-ray microcomputer tomography, which demonstrated that cracks are arrested by pores [51].

Finally, Fig. 9b shows the MFIS magnitude as a function of the magnetic field orientation for a full field rotation initial state, after first training, after first neutralization, after second training and after third training. The annealed foam (labeled "Initial" in Fig. 9b) shows a broad strain peak (0.1% MFIS) between −20° and 130° (and a corresponding peak between 160° and 310°) with an asymmetric shape, indicating the presence of multiple sub-peaks (and thus multiple variants), consistent with the polycrystalline nature of the foam. After the first magneto-mechanical training, a single peak (0.28% MFIS) with near-symmetrical shape peaking at 90/270° is visible, indicating a more homogeneous activation of twinning systems. Subsequent neutralization and training do not significantly alter the peak shape and angle.

3.5. Relation between foam architecture, grain size and bamboo grain structure

The struts may be compared to fibers with a bamboo microstructure. For such fibers, grains in which twins span

across the entire fiber exhibit large (local) MFIS, as recently reviewed [59]. Other grains, for which twin boundaries end at grain boundaries (and not at the surface), do not deform in a magnetic field. Thus, there are grain orientations favoring MFIS and others which disfavor MFIS.

In a foam where struts point in different directions, the orientation of the strut also affects the possibility to produce MFIS. Assume that the grain size corresponds to the pore size of the single-pore foam or to the size of the large pores of dual-pore foam. Then there will be many grains in the single-pore foam, for which twins will end at a grain boundary; these twins are blocked. For the dual-pore foam, the same twins will be separated from the grain boundaries by pores; thus, the twins end at free surfaces and are mobile (as in single crystals).

A similar argument may be developed for foam with larger grains where geometrical constraints may cause multiple twin variants in nodes of large pores/struts. These nodes would act like single crystals with self-accommodated martensite which do not display large MFIS [33]. The small pore population separates twins from such internally constraint regions and promote twin boundary motion.

Only foams with very small grain size, i.e. grains with sizes comparable to that of the small pores, will show suppression of twin boundary motion. As Figs. 5a and b show, this is not the case in the present foams. Thus, it is expected that the twins are more mobile in dual-pore foam than in single-pore foam, as found in the present experiments. The results presented here are consistent with common origins of size effects which arise due to the interaction of microstructural or architectural and mechanistic length scales [59,60].

4. Conclusions

This paper presents a comparison in MFIS between two polycrystalline Ni–Mn–Ga foams with pores exhibiting single and dual size. The following conclusions are reached:

– $NaAlO_2$ is a suitable space holder material for creation of Ni–Mn–Ga foams by melt infiltration of $NaAlO_2$ powders and subsequent acid removal, allowing the creation of pores with a single size or two sizes by using one or two powder sizes. Acid removal of the $NaAlO_2$ does not change the composition of the foam. The foam with dual size pores exhibits much thinner nodes and struts than the foam with single size pores. Martensite twins span the whole width of these thinner struts.
– Both foams show high MFIS values: 0.24% for the single-pore foam (in the annealed state) and 0.28% in the dual-pore foam (after training). This is consistent with a reduction of constraints provided by the pores, allowing easier movements of twins.
– The MFIS of both types of foams drops slowly over thousands of magneto-mechanical cycles probably due to damage accumulation. The dual-pore foam shows

lower rate of MFIS decrease, indicating that the finer pores reduce constraints and/or limit propagation of cracks.

References

[1] Enkovaara J, Ayuela A, Zayak AT, Entel P, Nordstrom L, Dube M, et al. Mater Sci Eng 2004;A378:52.
[2] Söderberg O, Ge Y, Sozinov A, Hannula SP, Lindroos VA. Smart Mater Struct 2005;14:S223.
[3] Wayman CM. MRS Bull 1993;18(4):49.
[4] Sarawate NN, Dapino MJ. Appl Phys Lett 2008;93:062501.
[5] Haertling GH. J Am Chem Soc 1999;82:797.
[6] Cullen JR, Clark AE, Hathaway KB. In: Buschow KHJ, editor. Handbook of materials science. Amsterdam: VCH; 1997.
[7] Kainuma R, Imano Y, Ito W, Sutou Y, Morito H, Okamoto S, et al. Nature 2006;439(7079):957.
[8] Lanvrov AN, Komiya S, Ando Y. Nature 2002;418(6896):385.
[9] Zhang JH, Peng WY, Hsu TH. Appl Phys Lett 2008;93:122510.
[10] James RD, Wuttig M. Philos Mag 1998;A77(5):1273.
[11] Ullakko K, Huang JK, Kantner C, O'Handley RC, Kokorin VV. Appl Phys Lett 1996;69(13):1966.
[12] Kiefer B, Karaca HE, Lagoudas DC, Karaman I. J Magn Magn Mater 2007;312:164.
[13] O'Handley RC. J Appl Phys 1998;83(6):3263.
[14] Sozinov A, Likhachev AA, Lanska N, Ullakko K. Appl Phys Lett 2002;80(10):1746.
[15] Vassiliev A. J Magn Magn Mater 2002;242–245:66.
[16] Pasquale M. Sens Actuators 2003;A106:142.
[17] Wilson SA, Jourdain RPJ, Zhang Q, Dorey RA, et al. Mater Sci Eng 2007;R56:1.
[18] Müllner P, Chernenko VA, Kostorz G. Scripta Mater 2003;49:129.
[19] Suorsa I, Tellinen J, Ullakko K, Pagounis E. J Appl Phys 2004;95(12):8054.
[20] Tickle R, James RD. J Magn Magn Mater 1997;195:627.
[21] Tickle R, James RD, Shield T, Wuttig M, Kokorin VC. IEEE Trans Magn 1999;35:4301.
[22] O'Handley RC, Murray SJ, Marioni M, Nembach H, Allen SM. J Appl Phys 2000;87(9):4712.
[23] Heczko O, Sozinov A, Ullakko K. IEEE Trans Magn 2000;36(5):3266.
[24] Murray SJ, Marioni M, Allen SM, O'Handley RC, Lograsso TA. Appl Phys Lett 2000;77(6):886.
[25] Müllner P, Chernenko VA, Kostorz G. J Appl Phys 2004;95(3):1531.
[26] Ullakko K, Huang JK, Kokorin VV, O'Handley RC. Scripta Mater 1997;36:1133.
[27] Sozinov A, Likhachev AA, Ullakko K. IEEE Trans Magn 2002;38(5):2814.
[28] Murry SJ, Marioni M, Tello PG, Allen SM, O'Handley RC. J Magn Magn Mater 2001;226–230:945.
[29] Müllner P, Chernenko VA, Wollgarten M, Kostorz G. J Appl Phys 2002;92(11):6708.

[30] Müllner P, Chernenko VA, Kostorz G. J Magn Magn Mater 2003;267:325.

[31] Boonyongmaneerat Y, Chmielus M, Dunand DC, Müllner P. Phys Rev Lett 2007;99:247201.

[32] Pasquale M, Sasso C, Besseghini S, Passaretti E, Villa E, Sciacca A. IEEE Trans Magn 2000;36(5):3263.

[33] Chmielus M, Chernenko VA, Knowlton WB, Kostorz G, Müllner P. Eur Phys J Spec Top 2008;158:79.

[34] Aaltio I, Söderberg O, Ge Y, Hannula SP. Scripta Mater 2010;62:9.

[35] Straka L, Lanska N, Ullakko K, Sozinov A. Appl Phys Lett 2010;96:131903.

[36] Lanska N, Söderberg O, Sozinov A, Ge Y, Ullakko K, Lindroos VK. J Appl Phys 2004;95(12):8074.

[37] Peterson BW, Allen SM, O'Handley RC. J Appl Phys 2008;104:033918.

[38] Heczko O, Straka L, Lanska N, Ullakko K, Enkovaara J. J Appl Phys 2002;91(10):8228.

[39] Okamoto N, Fukuda T, Kakeshita T. Mater Sci Eng 2008;A481–A482:306.

[40] Thompson CV. Annu Rev Mater Sci 2000;30:159.

[41] Marioni MA, O'Handley RC, Allen SM. J Appl Phys 2002;91:7807.

[42] Ullakko K, Ezer Y, Sozinov A, Kimmel G, Yakovenko P, Lindroos YK. Scripta Mater 2001;44:475.

[43] Liang T, Jiang CB, Xu HB, Liu ZH, Zhang M, Cui YT, et al. J Magn Magn Mater 2004;268:29.

[44] Gaitzsch U, Pötschke M, Roth S, Rellinghaus B, Schultz L. Acta Mater 2009;57:365.

[45] Pötschke M, Gaitzsch U, Roth S, Rellinghaus B, Schultz L. J Magn Magn Mater 2007;316:383.

[46] Gaitzsch U, Pötschke M, Roth S, Rellinghaus B, Schultz L. Scripta Mater 2007;57:493.

[47] Scheerbaum N, Heczko O, Liu J, Hinz D, Schultz L, Gutfleisch O. New J Phys 2008;10:073002.

[48] Kohl M, Agarwal A, Chernenko VA, Ohtsuka M, Seemann K. Mater Sci Eng 2006;A438–A440:940.

[49] Hathaway K, Clark AE. MRS Bull 1993;18(4):34.

[50] Chmielus M, Zhang XX, Witherspoon C, Dunand DC, Müllner P. Nat Mater 2009;8(11):863.

[51] Chmielus M, Witherspoon C, Wimpory R, Paulke A, Hilger A, Zhang XX, et al. J Appl Phys 2010;108:123526.

[52] Conde Y, Despois JF, Goodall R, Marmottant A, Salvo L, San Marchi C, et al. Adv Eng Mater 2006;8(9):795.

[53] Boonyongmaneerat Y, Dunand DC. Adv Eng Mater 2008;10(4):379.

[54] Müllner P, Kostorz G. Mater Sci Forum 2008;583:43.

[55] Seguí C, Cesari E, Pons J, Chernenko VA. Mater Sci Eng 2004;A370:481.

[56] Gutiérrez J, Barandiarán JM, Lázpita P, Seguí C, Cesari E. Sens Actuators 2006;A129:163.

[57] Heczko O, Straka L. J Appl Phys 2003;94:7139.

[58] Chernenko VA, L'vov VA, Khovailo VV, Takagi T, Kanomata T, Suzuki T, et al. J Phys: Condens Matter 2004;16:8345.

[59] Dunand DC, Müllner P. Adv Mater 2011;23:216.

[60] Arzt E. Acta Mater 1998;46:5611.